Supplementary Information (SI) for ChemComm.

# Electronic Supplementary Information

## Surface Pre-Oxidized Copper Foam-Derived Prussian Blue Analogue Heterointerface for Enhanced Anodic Oxidation Performance

Ayusie Goyal,[a] Shalini Verma,[a] Labham Singh,[a] Baghendra Singh,[a]* and Apparao Draksharapu[a]*

[a]Southern Laboratories - 208A, Department of Chemistry, Indian Institute of Technology Kanpur, Kanpur-208016 (India).

E-mail: baghendras@iitk.ac.in, appud@iitk.ac.in

## EXPERIMENTAL SECTION

### Chemicals

The catalyst synthesis was carried out using high-purity analytical-grade chemicals, which were used as received without further treatment. Copper foam was sourced from Kanopy Techno Solutions Pvt. Ltd., Pune, India. Double-distilled water was utilized for both synthesis and electrochemical measurements. The following reagents were obtained from Sisco Research Laboratories Pvt. Ltd.: Potassium ferricyanide extrapure ($K_3[Fe(CN)_6]$), cobalt(II) chloride hexahydrate ($CoCl_2 \cdot 6H_2O$), sodium hydroxide (NaOH), sodium persulfate ($Na_2S_2O_8$)

### Instruments

The synthesized materials were characterized using various analytical techniques. Powder X-ray diffraction (PXRD) was conducted using a PANalytical Xpert powder diffractometer to determine the phase composition and crystal structure. The analysis was carried out using Cu-$K_\alpha$ radiation ($\lambda = 0.154$ nm) within a $2\theta$ range of 5° to 80°, employing a step size of 0.01°. X-ray photoelectron spectroscopy (XPS) was performed to investigate the valence states of the constituent elements, utilizing a PHI 5000 Versa Probe II system. The XPS was directly on the copper foam, having deposited samples. Data fitting was conducted using Origin Pro 8.5. Fourier transform infrared (FT-IR) spectra were acquired in attenuated total reflectance (ATR) mode. The morphological characteristics of the materials were analyzed using a field emission scanning electron microscope (FE-SEM) with a JEOL JSM-6010LA tungsten electron source (W-SEM). Transmission electron microscopy (TEM) imaging was conducted using a Tecnai G2 20 TWIN electron microscope. Elemental distribution was analyzed through energy-dispersive X-ray (EDX) mapping integrated with the SEM system.

### Electrochemical Measurements

The electrochemical performance of the catalyst was assessed using a CHI-610E electrochemical workstation in a three-electrode configuration. An Ag/AgCl electrode was utilized as the reference electrode, a platinum (Pt) wire functioned as the counter electrode, and the catalysts were used as the working electrode. For the benzyl alcohol oxidation, the LSV (reverse scan) was carried out in 1.0 M aqueous KOH with/without 0.1 M benzyl alcohol solution and plotted with 70% iR compensation. The potential was presented against the reversible hydrogen electrode (RHE) by the following equation:

$$E(RHE) = E(Ag/AgCl) + 0.197 + 0.059pH$$

Electrochemical impedance spectroscopy (EIS) measurements were conducted over a frequency range of 0.01 to 100,000 Hz with an applied amplitude of 10 mV. The charge transfer resistance ($R_{ct}$) values were determined from the diameter of the semicircle in the Nyquist plots. Chronoamperometric (CA) measurements were performed in a 1.0 M KOH solution with 0.1 M benzyl alcohol at a fixed potential, with results presented without iR compensation. The Tafel slope was calculated from LSV curves. Cyclic voltammetry (CV) for the determination of double-layer capacitance ($C_{dl}$) was carried out within a potential range where no significant faradaic processes were observed.

## Activation of copper foam (CF)

Copper foam (1 cm × 2 cm) was first cleaned with acetone, followed by repeated rinsing with double-distilled water. The cleaned foams were then sonicated in 1.0 M HCl for 10 minutes, thoroughly washed with double-distilled water, and subsequently dried in an oven at 50 °C for 12 hours.

## Surface pre-oxidation of CF (A-CF)

A solution of 0.5 mmol $Na_2S_2O_8$ was prepared in 5 mL of 2.0 M aqueous NaOH in a glass vial. The activated CF films were immersed vertically in the solution, exposing a 1 $cm^2$ area inside the solution, and kept undisturbed for 30 minutes at room temperature. After the treatment, the surface pre-oxidized CF films were thoroughly washed with distilled water and dried in an oven at 50 °C for 12 hours.

## Synthesis of CoFe-PBA@A-CF

A solution (**A**) was prepared by dissolving 1.5 mmol of $CoCl_2 \cdot 6H_2O$ in 3 mL of double-distilled water, while another solution (**B**) was obtained by dissolving 1.0 mmol of $K_3[Fe(CN)_6]$ in 3 mL of double-distilled water. Solution **B** was then gradually added to solution **A** to synthesize CoFe-PBA. A surface pre-oxidized CF (**A-CF**) film was immersed vertically in the CoFe-PBA solution and left undisturbed for 6 hours at room temperature. The resulting CoFe-PBA@A-CF films were thoroughly washed with distilled water and dried at 50 °C for 12 hours.

## Synthesis of CoFe-PBA@CF

To synthesize CoFe-PBA, solution (**A**) was first prepared by dissolving 1.5 mmol of $CoCl_2 \cdot 6H_2O$ in 3 mL of double-distilled water, while solution (**B**) was obtained by dissolving

1.0 mmol of $K_3[Fe(CN)_6]$ in 3 mL of double-distilled water. Solution **B** was then gradually added to solution A with continuous stirring, facilitating the formation of CoFe-PBA. A CF film without surface pre-oxidation was immersed in the solution for 6 hours at room temperature. The resulting CoFe-PBA@CF film was then thoroughly washed with distilled water and dried in an oven at 50 °C for 12 hours.

### Determination of Faradaic Efficiency for BA Oxidation[1]

The Faradaic efficiency for benzyl alcohol (BA) oxidation was evaluated based on the mass of BA and the total charge passed during the electrocatalytic reaction. Complete conversion of BA to benzoic acid was confirmed by $^1$H NMR spectroscopy, allowing the theoretical charge required for complete oxidation ($Q_{100\%\ FE}$) to be determined using the equation:

$$\mathbf{Q_{100\%\ FE}} = \frac{\mathbf{m_{BA} \times F \times n_e}}{\mathbf{M_{BA}}}$$

Where F is the Faraday constant (96,485 C $mol^{-1}$), $n_e$ represents the number of electrons involved in the oxidation process (4), $m_{BA}$ is the initial mass of BA used (112.32 mg), and $M_{BA}$ is the molar mass of BA (108.14 g $mol^{-1}$). Based on this calculation, $Q_{100\%\ FE}$ was found to be 400.85 C. Considering the 99% purity of the BA sample (Alfa Aesar), the theoretical charge was adjusted to 396.84 C. After 6 hours of electrolysis, the actual charge recorded via the potentiostat was 386.10 C, leading to a calculated Faradaic efficiency of 97.2%.

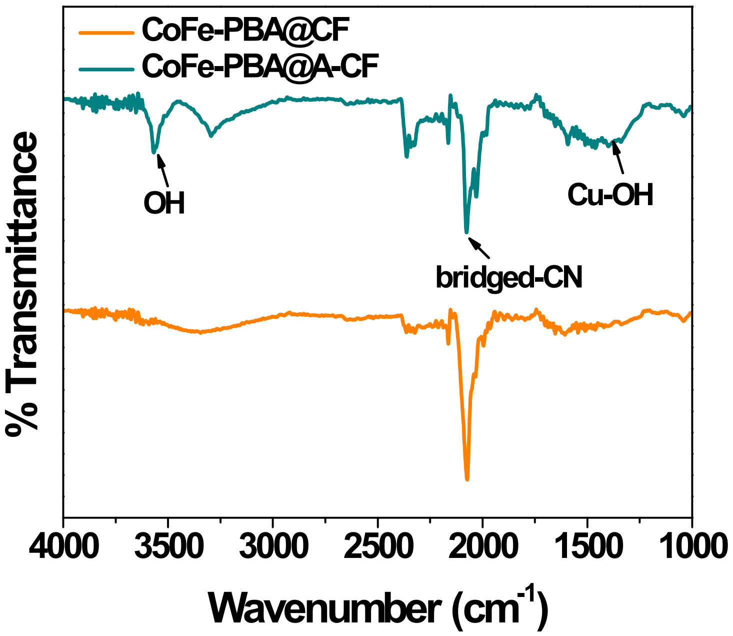

**Figure S1.** Infrared (IR) spectra of CoFe-PBA@CF and CoFe-PBA@A-CF. The spectrum of CoFe-PBA@CF exhibits a characteristic peak at 2073 cm$^{-1}$, corresponding to a metal-coordinated -C≡N bridge.[2,3] In contrast, CoFe-PBA@A-CF shows additional peaks at 1371 cm$^{-1}$ and 3565 cm$^{-1}$, attributed to the Cu–OH bond (in-plane bending vibration) and free -OH group, respectively, along with the bridging -C≡N peak at 2075 cm$^{-1}$.

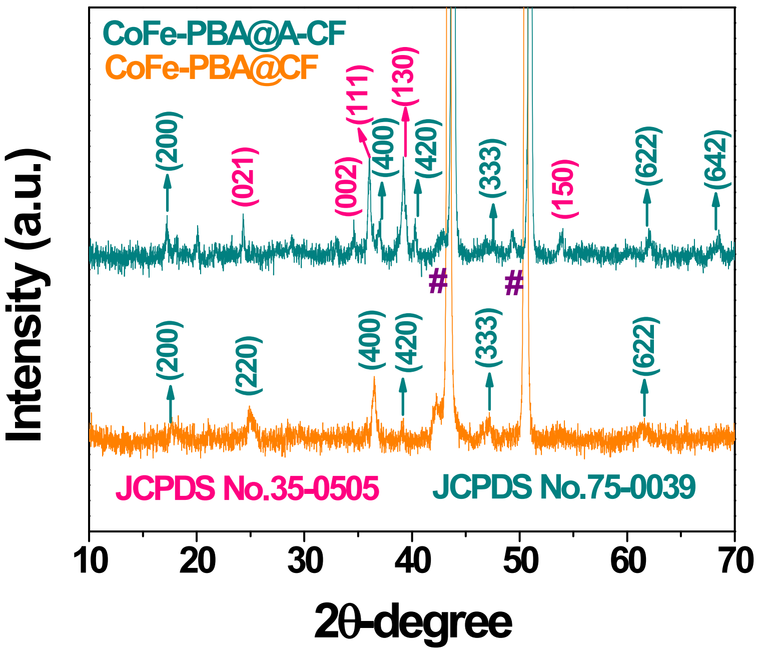

**Figure S2.** PXRD patterns of CoFe-PBA@CF and CoFe-PBA@A-CF. The CoFe-PBA@CF exhibits peaks corresponding to the cubic phase of CoFe-PBA (JCPDS No. 75-0039), while CoFe-PBA@A-CF shows additional peaks associated with the α-phase of $Cu(OH)_2$ (JCPDS No. 35-0505).

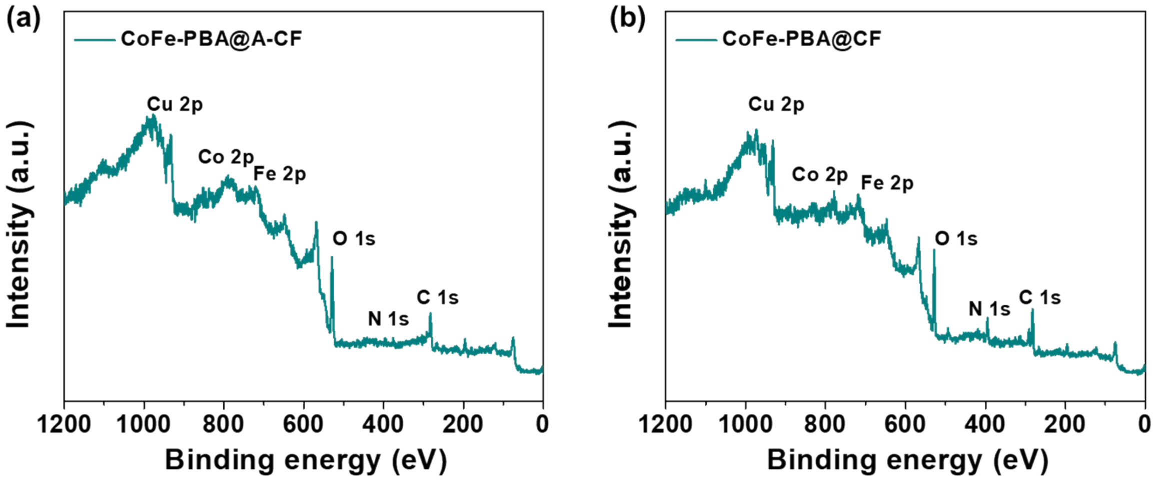

**Figure S3.** (a) XPS survey spectra of CoFe-PBA@A-CF; and (b) XPS survey spectra of CoFe-PBA@CF.

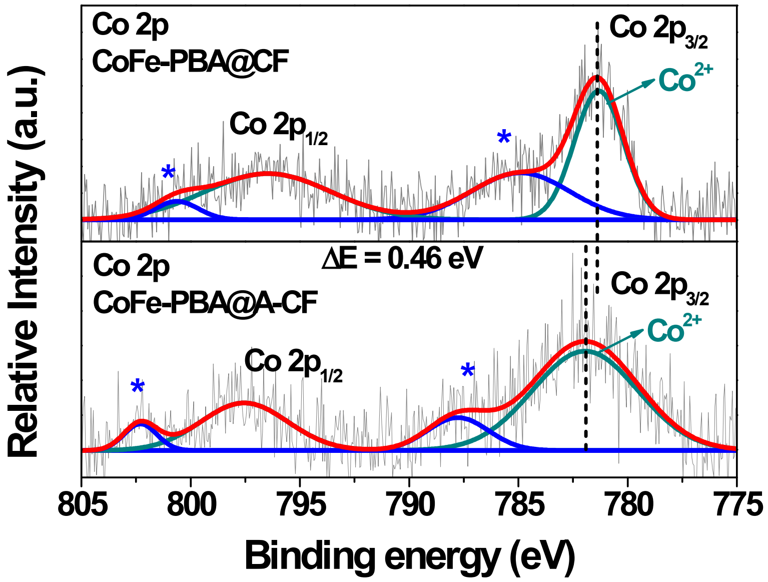

**Figure S4.** Co 2p XPS spectra of CoFe-PBA@CF and CoFe-PBA@A-CF. The CoFe-PBA@A-CF spectrum exhibits two main peaks corresponding to Co $2p_{3/2}$ and Co $2p_{1/2}$, with deconvolution of the Co $2p_{3/2}$ peak revealing a signal at 781.90 eV, attributed to $Co^{2+}$ species. A positive shift of 0.46 eV in the Co $2p_{3/2}$ peak is observed for CoFe-PBA@A-CF compared to CoFe-PBA@CF, indicating electronic structure modifications. The * marked peaks are assigned for the satellite peaks.[4–6] Satellite peaks in Co 2p and Fe 2p XPS spectra arise due to shake-up and multiplet splitting effects, which are common in transition metal ions with partially filled d-orbitals. In Co and Fe, when a core-level electron is ejected during XPS measurement, the valence electrons can undergo an energy loss process known as shake-up. This occurs because the sudden creation of a core hole perturbs the electron cloud, exciting a valence electron to a higher energy level. The result is an additional peak at a higher binding energy than the main peak.

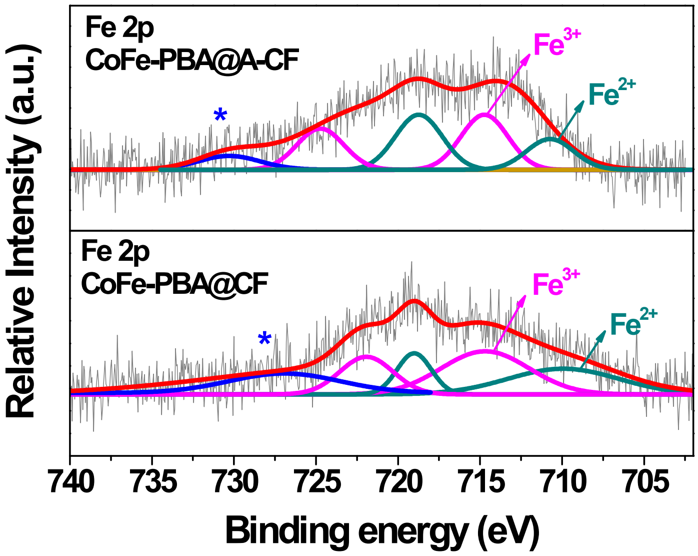

**Figure S5.** Fe 2p XPS spectra of CoFe-PBA@CF and CoFe-PBA@A-CF. The CoFe-PBA@A-CF spectrum exhibits the peaks corresponding to $Fe^{2+}$ and $Fe^{3+}$, with binding energies at 710.75 eV and 714.69 eV. A positive shift of 0.92 eV in the $Fe^{2+}$ peak is observed for CoFe-PBA@A-CF compared to CoFe-PBA@CF. The * marked peaks are assigned for the satellite peaks.[7,8]

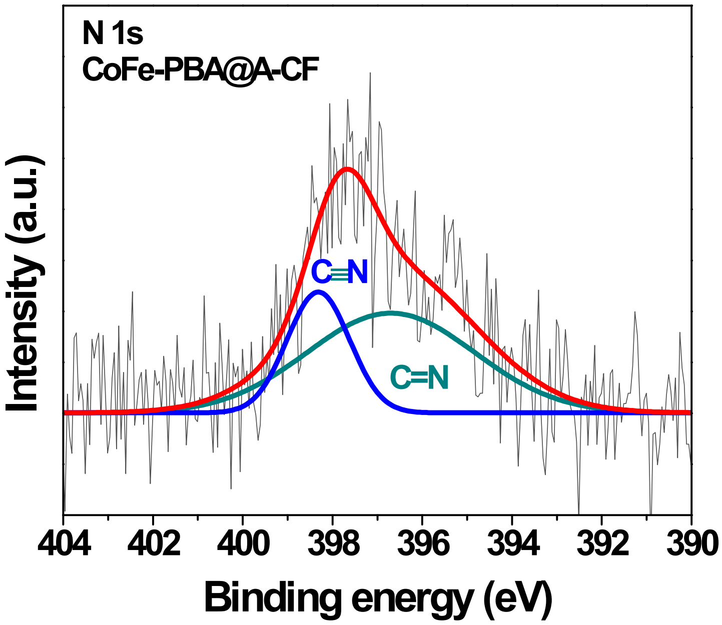

**Figure S6.** N 1s XPS spectrum of CoFe-PBA@A-CF. The spectrum exhibits two distinct peaks at 397.71 eV and 398.31 eV, corresponding to C=N and C≡N bonds, respectively, confirming the presence of -CN bridging within the PBA framework. The N 1s spectrum of CoFe-PBA@CF shows a negative shift of 0.31 eV compared to CoFe-PBA@A-CF.[4–6]

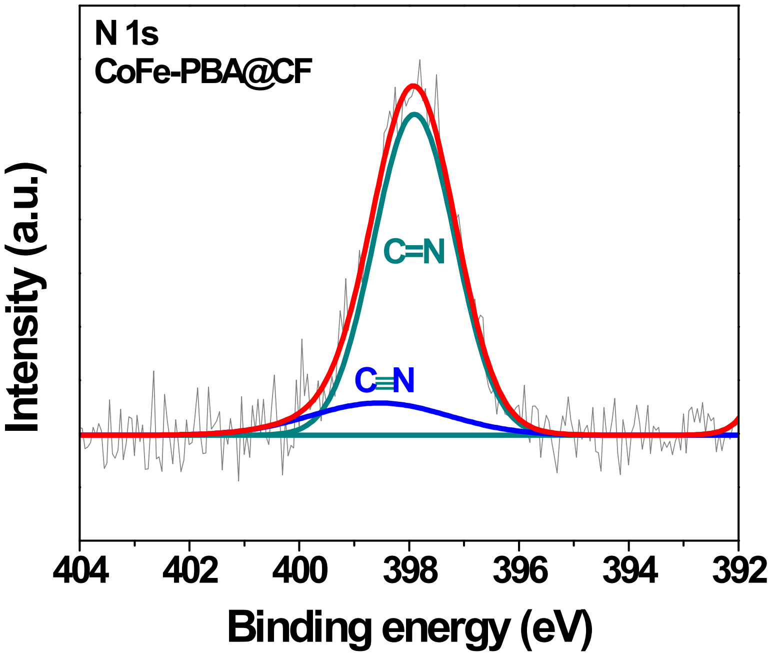

**Figure S7.** N 1s XPS spectrum of CoFe-PBA@CF. The spectrum exhibits two distinct peaks at 397.77 eV and 398.55 eV, corresponding to C=N and C≡N bonds, respectively, confirming the presence of -CN bridging within the PBA framework.[4–6]

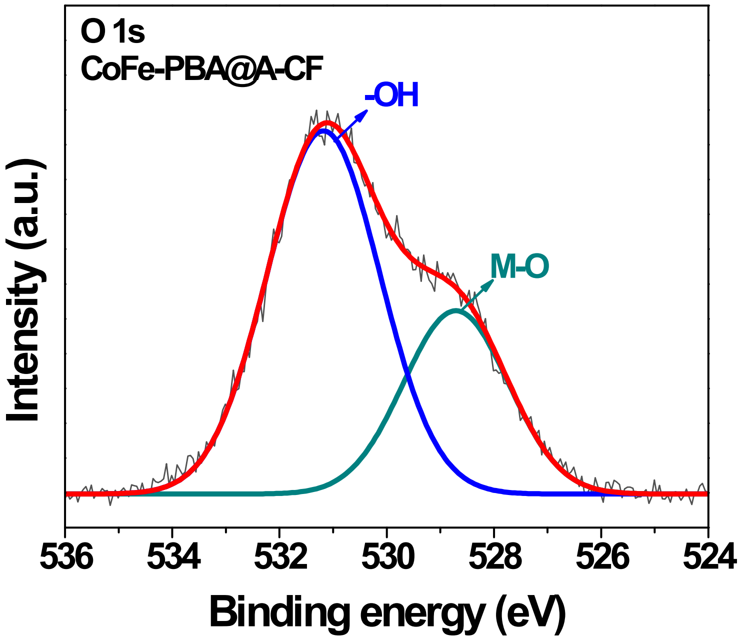

**Figure S8.** O 1s XPS spectrum of CoFe-PBA@A-CF. The spectrum displays two distinct peaks at 528.73 eV and 531.19 eV, attributed to the M–O bond and surface –OH groups, respectively. The peak for -OH groups was observed to be shifted at higher binding energy by 0.60 eV compared to CoFe-PBA@CF.[4–6]

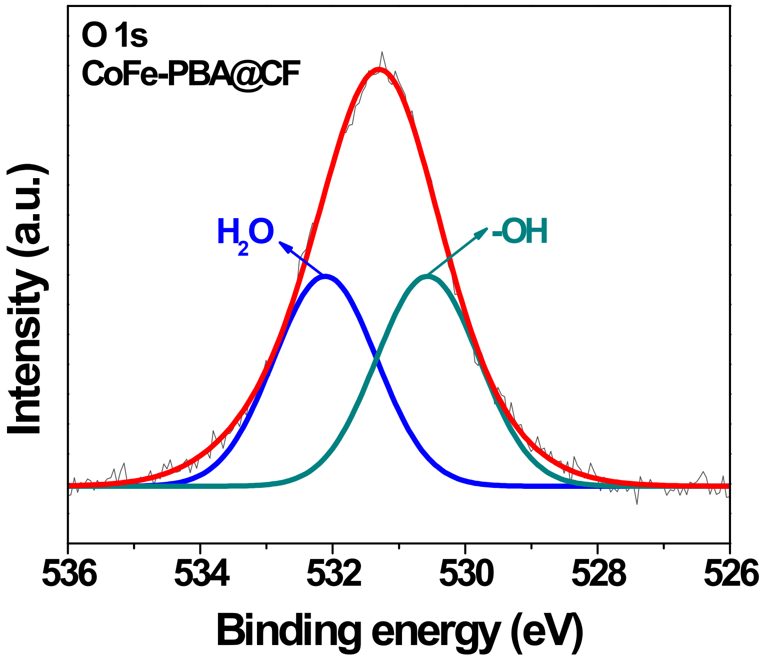

**Figure S9.** O 1s XPS spectrum of CoFe-PBA@CF. The spectrum displays two distinct peaks at 532.11 eV and 530.55 eV, respectively, attributed to the adsorbed water molecules and surface-OH groups.[4–6]

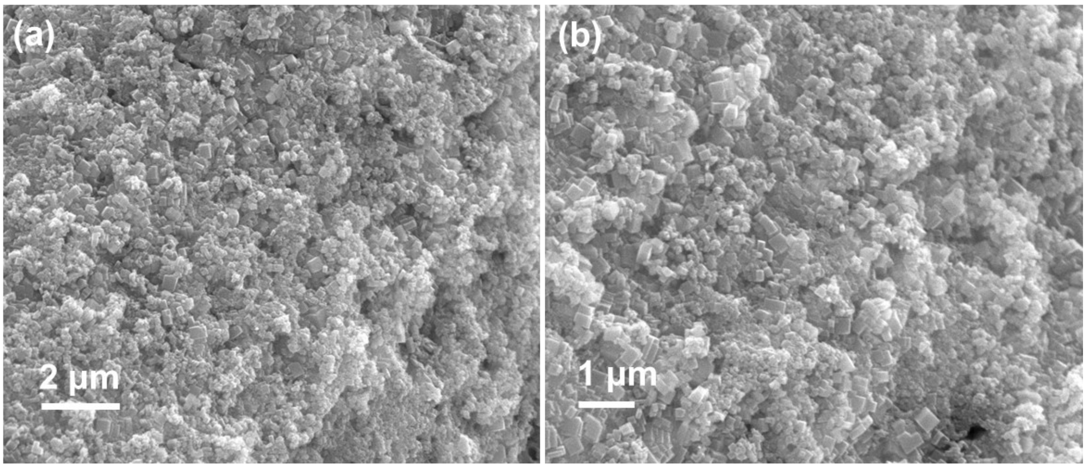

**Figure S10.** (a-b) SEM images of CoFe-PBA@CF showing the cubic morphology of the PBAs.

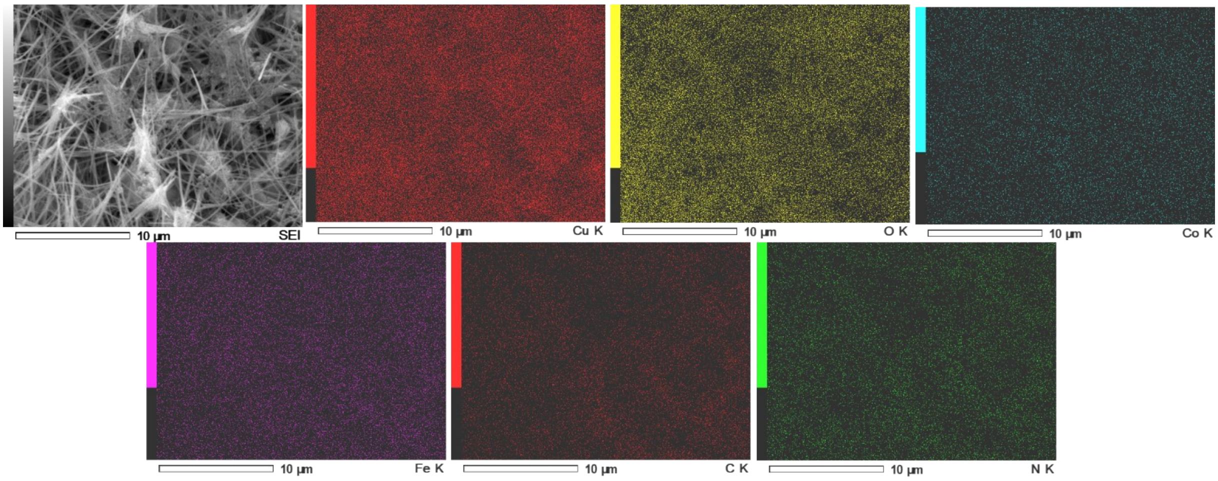

**Figure S11.** Energy dispersive X-ray elemental mapping images of CoFe-PBA@A-CF showing the uniform distribution of elements.

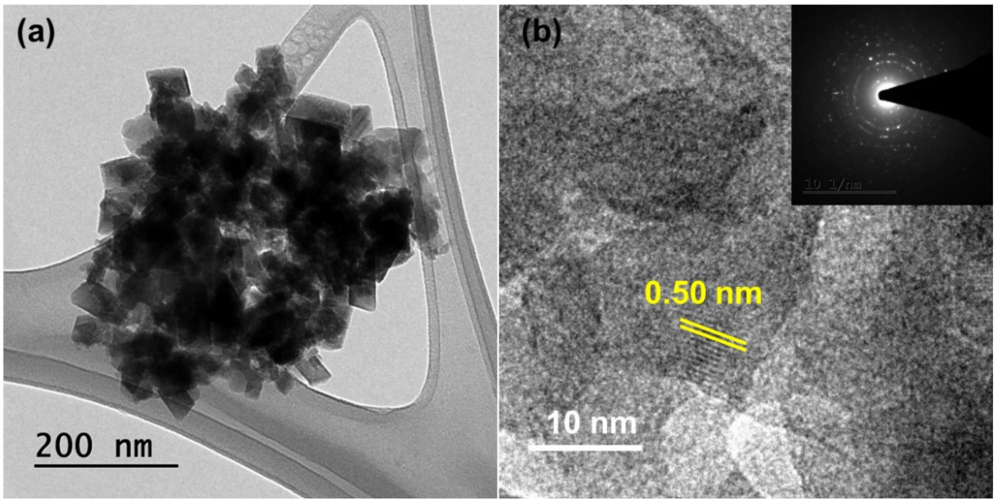

**Figure S12.** (a) TEM image of CoFe-PBA@CF; and (b) corresponding HRTEM image showing the 0.50 nm d-spacing for (200) plane of PBA (SAED inset).

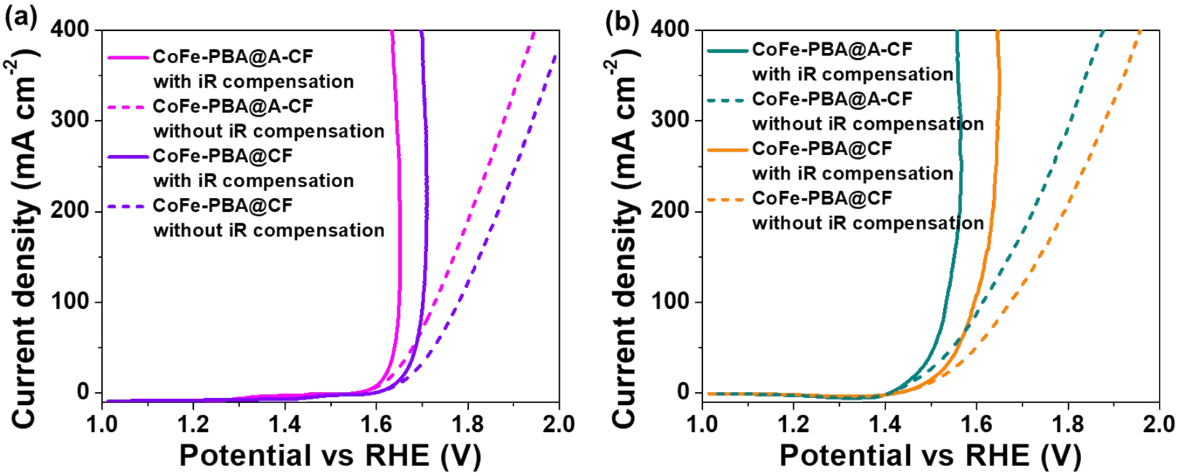

**Figure S13.** (a) OER-LSV profiles of the synthesized catalysts with and without iR compensation; and (b) BAOR-LSV profiles of the synthesized catalysts with and without iR compensation

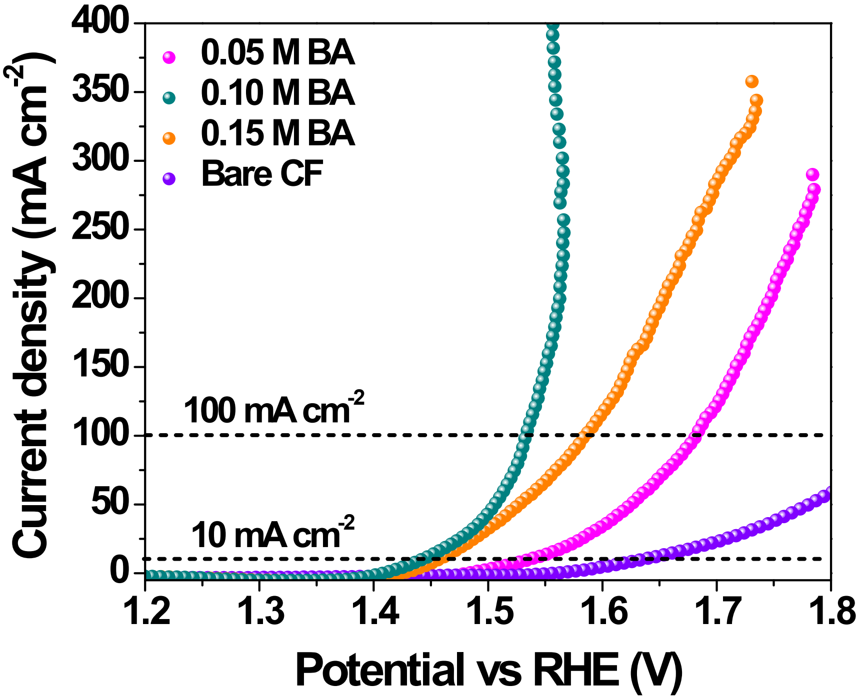

**Figure S14.** LSV profiles for the BAOR activity of CoFe-PBA@A-CF in 1.0 M KOH electrolyte having 0.05 M, 0.10 M, and 0.15 M benzyl alcohol.

**Table S1.** Comparison of the BA oxidation activity of CoFe-PBA@A-CF with literature-reported catalysts.

| Sr. No. | Catalyst | Potential | Current density | Faradaic efficiency | Reference |
|---|---|---|---|---|---|
| *1.* | *CoFe-PBA@A-CF* | *1.55 V vs RHE* | *400 mA cm$^{-2}$* | *97.2%* | *This work* |
| 2. | CoFe$O_x$ | 1.42 V vs RHE | 50 mA cm$^{-2}$ | 95% | *ACS Energy Lett.* **2018**, *3*, 1854-1860. |
| 3. | $Co_{0.83}Ni_{0.17}$/AC | 1.425 V vs RHE | 10 mA cm$^{-2}$ | 96% | *New J. Chem.* **2018**, *42*, 6381-6388. |
| 4. | $Co_3O_4$ | 1.50 V vs RHE | 86 mA cm$^{-2}$ | 91.4% | *J. Mater. Sci.* **2021**, *56*, 6689-6703. |
| 5. | NiCo-21-MOF | 1.52 V vs RHE | 338.16 mA cm$^{-2}$ | - | *Inorg. Chem.* **2022**, *61*, 7308-7317. |
| 6. | ZIF-9@GO | 1.60 V vs RHE | 204 mA cm$^{-2}$ | 88% | *J. Mater. Chem. A* **2024**, *12*, 233-246. |
| 7. | NiO/$Ni_3S_2$ | 1.609 V vs RHE | 50 mA cm$^{-2}$ | 94% | *Chem. Eng. J.* **2022**, *431*, 134137. |
| 8. | NC@$CuCo_2N_x$ | 1.25 V vs RHE | 10 mA cm$^{-2}$ | 81.3% | *Adv. Funct. Mater.* **2017**, 1704169 |
| 9. | $Ni_2P$ | 1.30 V vs RHE | 10 mA cm$^{-2}$ | 95.3% | *J. Colloid Interface Sci.* **2023**, *640*, 329-337. |
| 10. | $NiCo_2O_4$ | 1.46 V vs RHE | 100 mA cm$^{-2}$ | 99% | *Inorg. Chem. Front.* **2023**, *10*, 2053-2059. |
| 11. | Ni@Ni/Ni$O_x$ | 1.309 V vs RHE | 10 mA cm$^{-2}$ | 96% | *Chem. Eng. J.* **2023**, *453*, 139797. |
| 12. | NiCo-hydroxide | 1.35 V vs RHE | 100 mA cm$^{-2}$ | 95% | *Energy Environ. Sci.* **2020**, *13*, 4990-4999. |
| 13. | $ZnCo_2O_4$ @$Ni(OH)_2$ | 1.48V vs RHE | 100 mA cm$^{-2}$ | 96% | *Int. J. Hydro. Energy* **2024**, *49*, 228-237. |

**Equation S1.** Calculation of the energy efficiency during BAOR and OER.[1]

**For OER:**

$$Energy\ required = \frac{Voltage\ (V) \times Current\ (mA)}{H_2\ production\ rate\ \left({}^{L}/_{h}\right)}$$

$$Energy\ required = \frac{2.04 \times 100\ (VmA)}{0.0535\ \left({}^{L}/_{h}\right)} = \frac{2.04 \times 100 \times 10^{-3}\ (VA)}{0.0535 \times 10^{-3} \left({}^{m^3}/_{h}\right)}$$

= 3813.0 Wh/m$^3$ H$_2$ = 3.81 kWh/m$^3$ H$_2$

**For BAOR:**

$$Energy\ required = \frac{Voltage\ (V) \times Current\ (mA)}{H_2\ production\ rate\ \left({}^{L}/_{h}\right)}$$

$$Energy\ required = \frac{1.90 \times 100\ (VmA)}{0.1392\ \left({}^{L}/_{h}\right)} = \frac{1.90 \times 100 \times 10^{-3}\ (VA)}{0.1392\ \times 10^{-3} \left({}^{m^3}/_{h}\right)}$$

= 1364.9 Wh/m$^3$ H$_2$ = 1.36 kWh/m$^3$ H$_2$

**Economic Feasibility of BAOR**

The BAOR process occurs at a very low cell voltage compared to conventional water splitting due to the lower oxidation potential of benzyl alcohol than that of water. Hence the energy consumption required during BAOR is relatively less compared to conventional water splitting. Additionally, hydrogen production during BAOR is observed to improve by 2.6 times compared to OER. This makes the BAOR economically viable for large-scale hydrogen production. However, in industries where benzyl alcohol is a byproduct (e.g., pharmaceuticals, perfumery, and resin production), BAOR can serve as a value-added strategy by converting waste into valuable products like benzoic acid. The oxidation of benzyl alcohol to benzoic acid can generate economic benefits, as benzoic acid is widely used in food preservation, pharmaceuticals, and chemical industries. If integrated into industrial waste valorization, BAOR can be cost-effective. Moreover, the electrocatalytic BAOR is a very clean and green approach as it does not include the strong oxidant and highly toxic chemicals used in industries to oxidize benzyl alcohol to benzoic acid

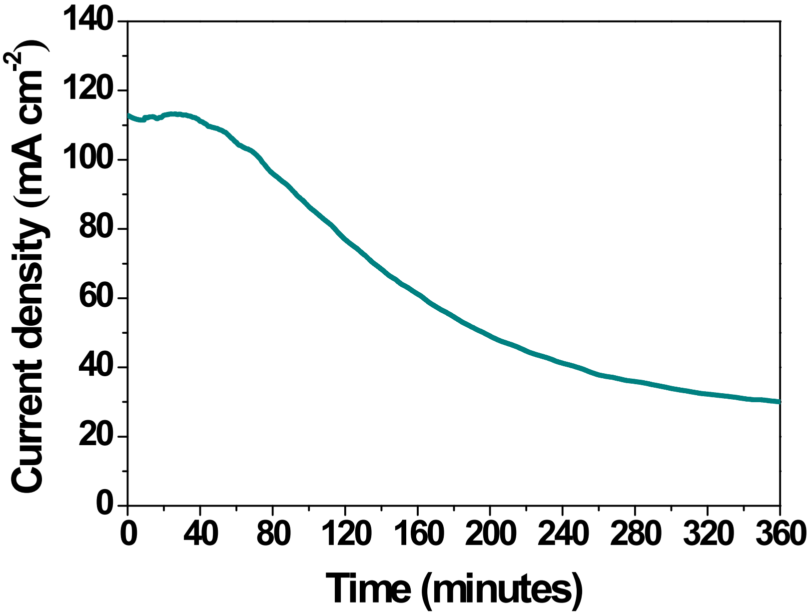

**Figure S15.** The chronoamperometric curve for the BA-oxidation at 1.55 V vs RHE using CoFe-PBA@A-CF.

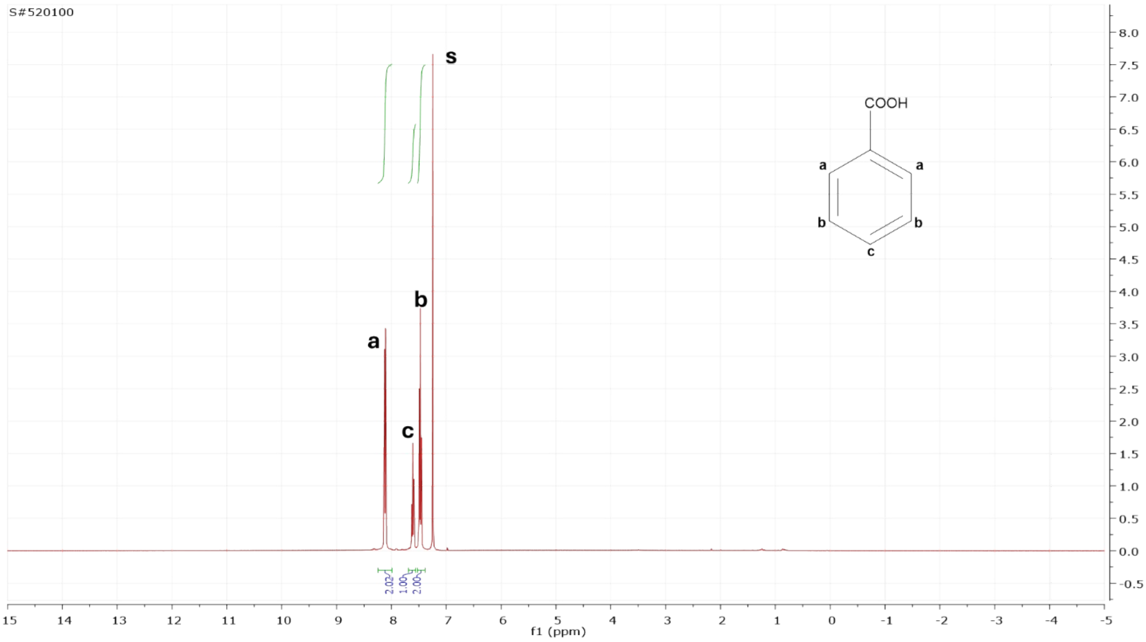

**Figure S16.** $^{1}H$ NMR spectrum (400 MHz) of benzoic acid formed after 6 h of BAOR using CoFe-PBA@A-CF. The peak ‘s’ is denoted for the solvent $CDCl_3$.

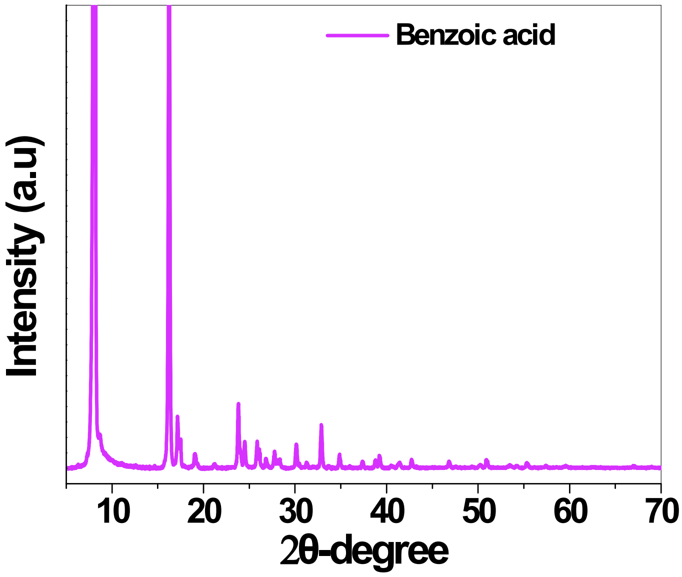

**Figure S17.** PXRD data of benzoic acid crystals formed after 6 h of BAOR using CoFe-PBA@A-CF. The PXRD pattern is matched with JCPDS No. 12-0853.

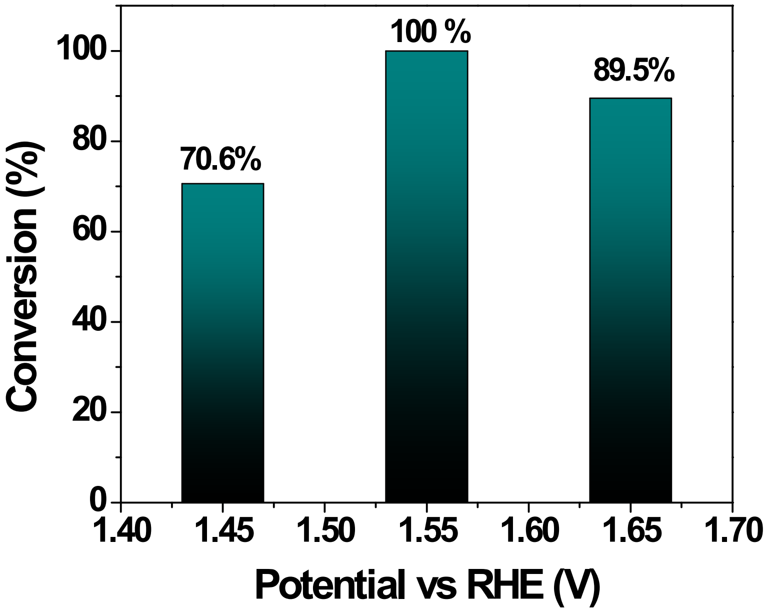

**Figure S18.** Potential dependent conversion of benzyl alcohol to benzoic acid using CoFe-PBA@A-CF.

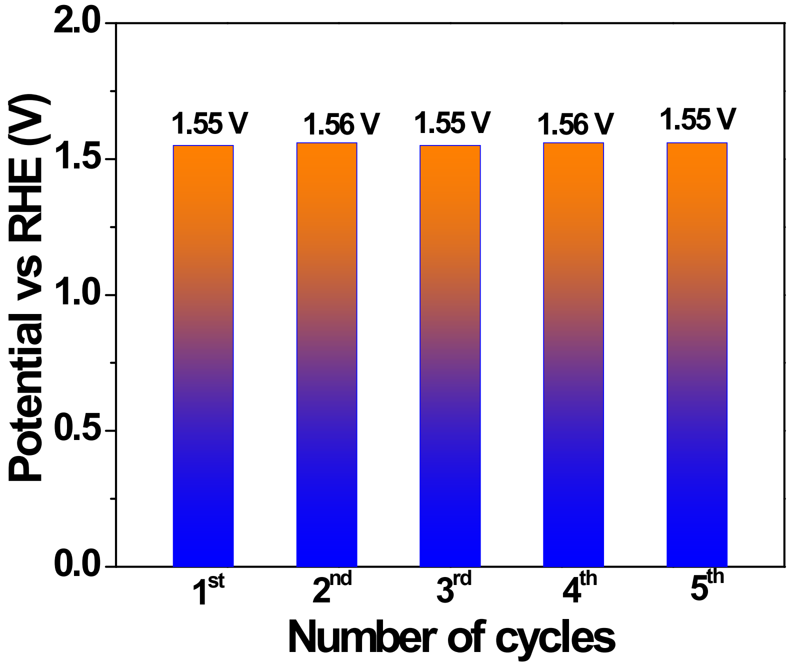

**Figure S19.** Cyclic stability CoFe-PBA@A-CF for BAOR shows no significant change in the potential for five consecutive cycles.

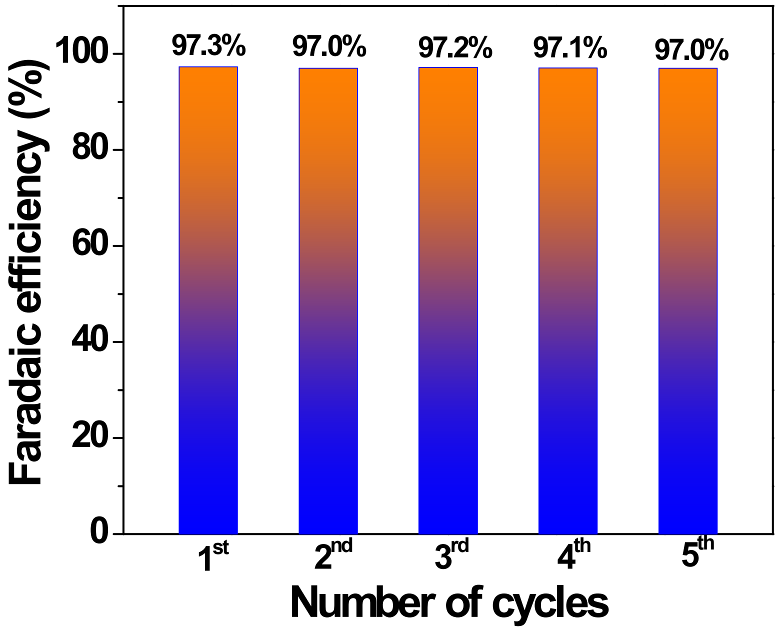

**Figure S20.** Faradaic efficiency (FE) measurement for BAOR using CoFe-PBA@A-CF showed no significant change in the FE for five consecutive cycles.

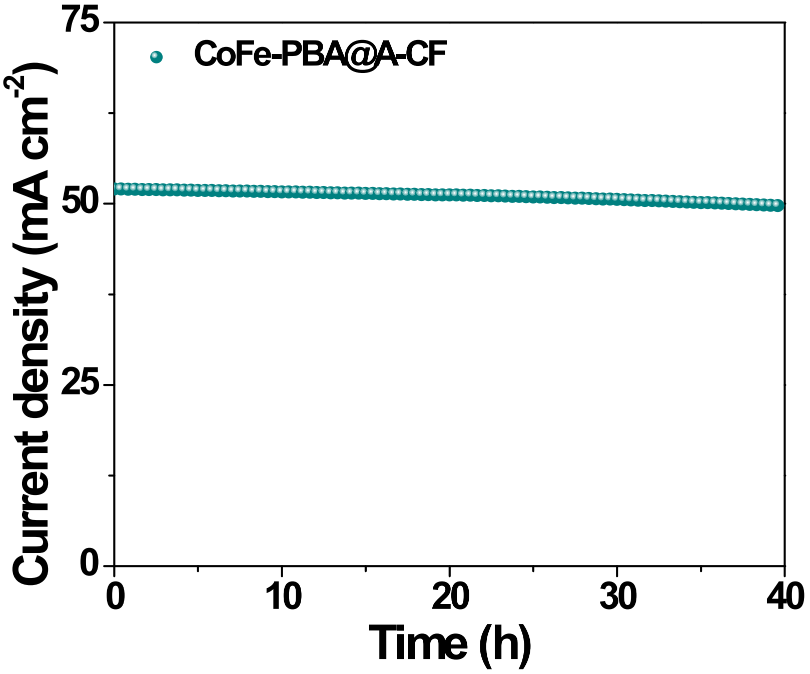

**Figure S21.** Chronoamperometric stability test of CoFe-PBA@A-CF for 40 h at 50 mA cm$^{-2}$ current density (electrolyte 1.0 M KOH + 0.1 M benzyl alcohol).

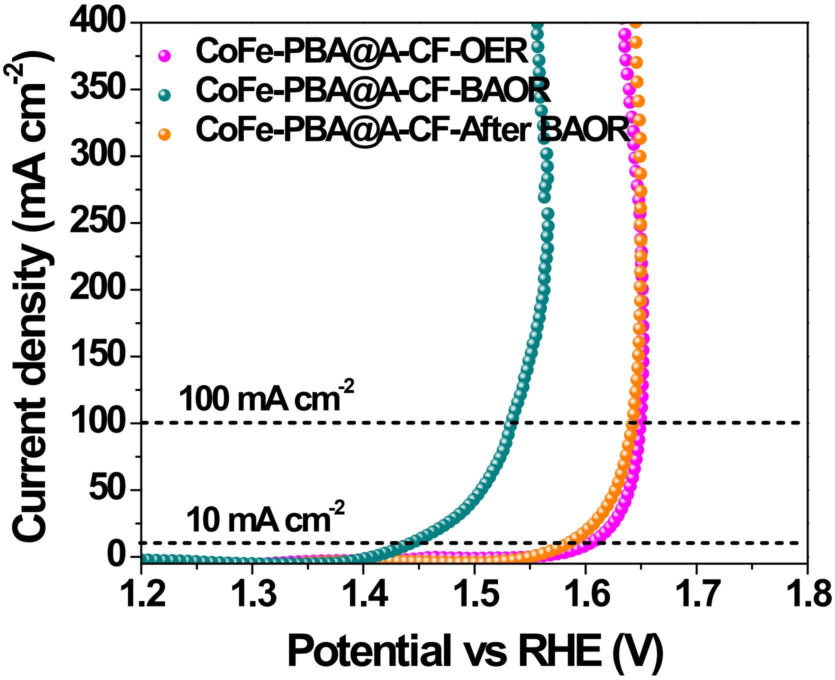

**Figure S22.** LSV profiles of CoFe-PBA@A-CF for OER, BAOR, and after 6 h of BAOR.

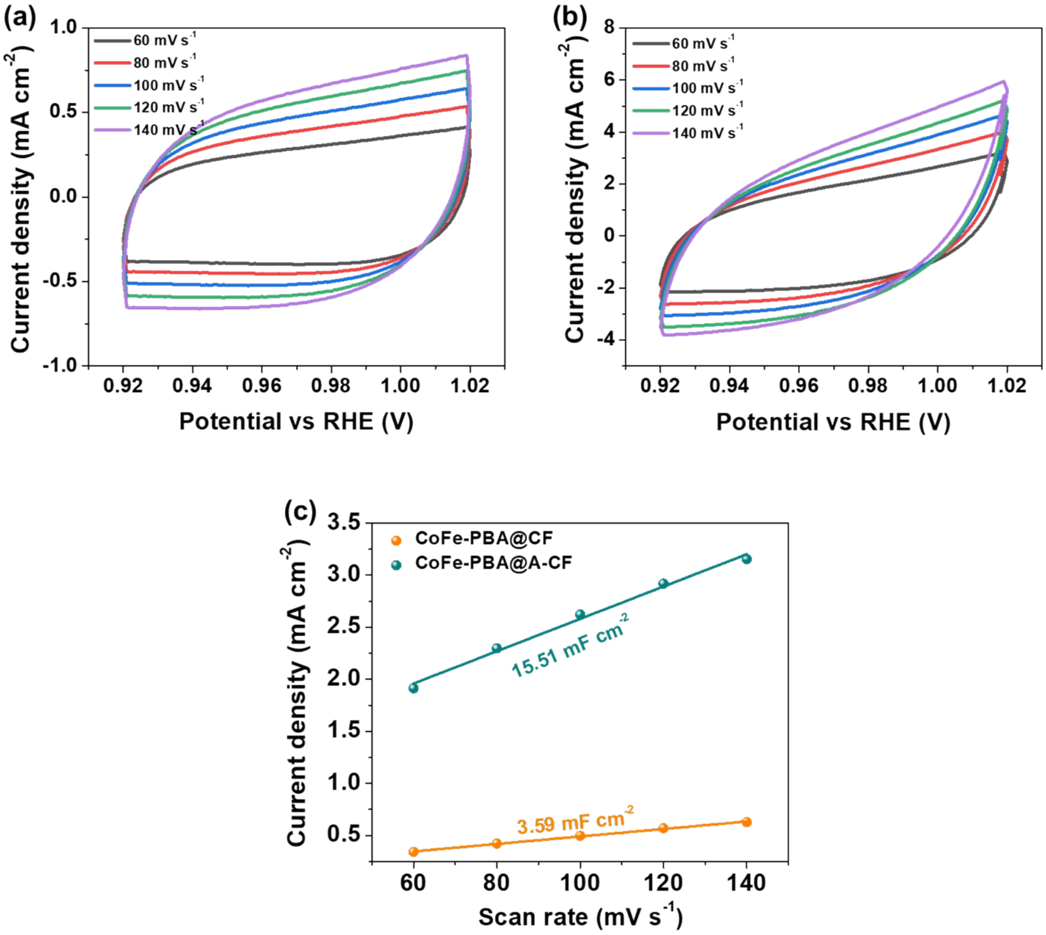

**Figure S23.** Electrochemical capacitance current of (a) CoFe-PBA@CF and (b) CoFe-PBA@A-CF within the non-Faradaic potential range of 0.92 V to 1.02 V vs. RHE, and (c) determination of the double-layer capacitance ($C_{dl}$) by plotting the half difference in current density against the scan rate.

Heterogeneous interfaces play a crucial role in improving charge transfer and reaction kinetics in electrocatalysis. At the interface of two different materials, electronic interactions can induce charge redistribution, altering the reactive sites. This tuning can optimize the adsorption energy of key intermediates, enhancing reaction kinetics. A built-in electric field at the heterointerface can promote directional charge transfer, reducing resistance and enhancing conductivity. This accelerates electron transport, decreasing the overpotential required for catalysis. Different components at the interface may have complementary catalytic properties. One material may facilitate reactant adsorption while the other accelerates intermediate conversion, leading to an overall improvement in activity. Defects and lattice mismatches at the heterointerface can create highly active sites with unique coordination environments, increasing catalytic efficiency. These effects can modify the reaction pathway, making the formation and desorption of intermediates more favourable.

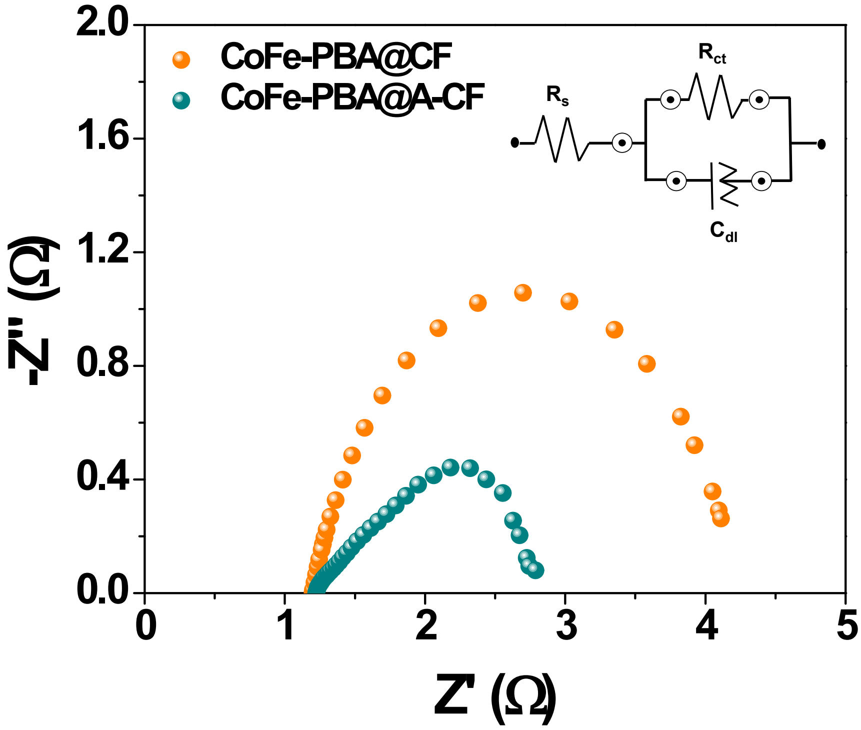

**Figure S24.** EIS spectra of CoFe-PBA@A-CF and CoFe-PBA@CF. Lower $R_{ct}$ values were observed for CoFe-PBA@A-CF.

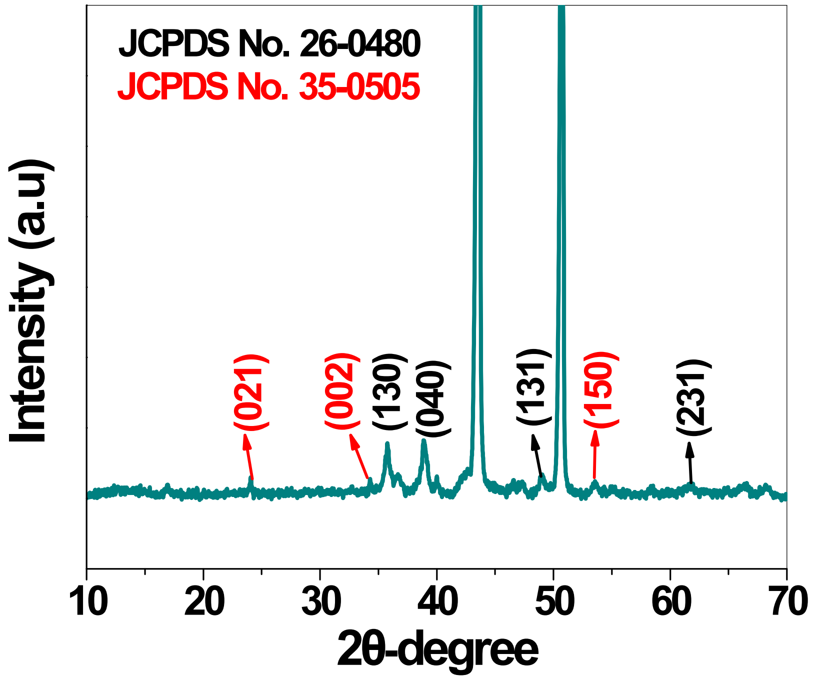

**Figure S25.** PXRD data of CoFe-PBA@A-CF after BAOR showing the formation of the mixed phase of alpha phase of $Cu(OH)_2$ (JCPDS No. 35-0505), alongside the characteristic peaks of Co(O)OH (JCPDS No. 26-0480).

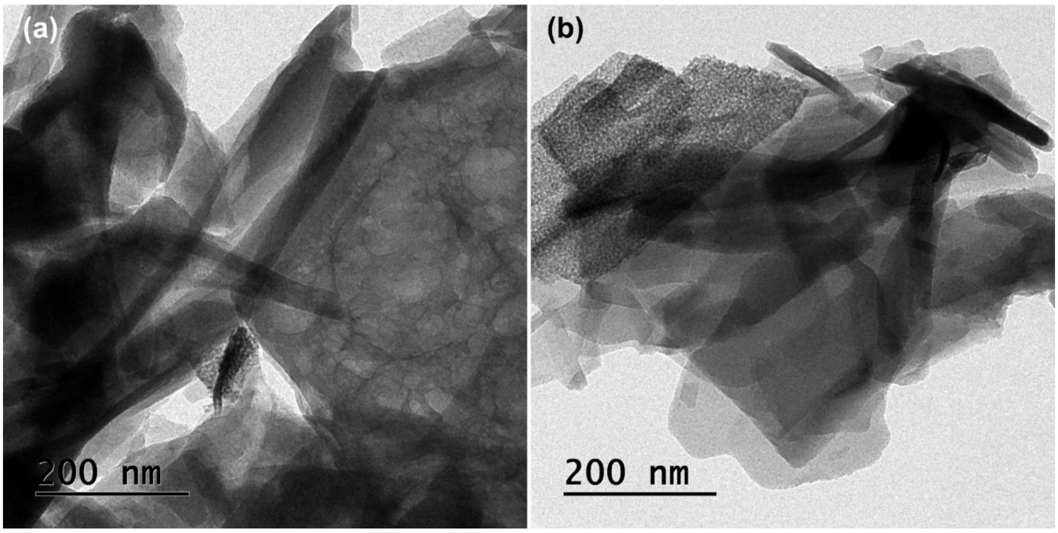

**Figure S26.** (a-b) TEM images of CoFe-PBA@A-CF after BAOR show the formation of nanosheets.

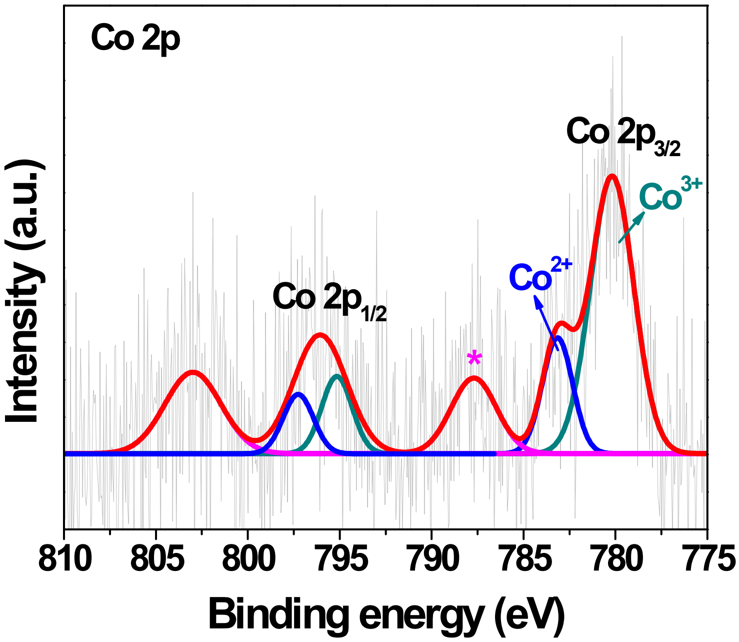

**Figure S27.** Co 2p XPS spectrum of CoFe-PBA@A-CF after BA-oxidation. The spectrum exhibits two prominent peaks corresponding to Co $2p_{3/2}$ and Co $2p_{1/2}$, with deconvolution of the Co $2p_{3/2}$ peak revealing two signals at 780.20 eV and 783.21 eV, attributed to $Co^{3+}$ and $Co^{2+}$ species, respectively. The origin of a peak for $Co^{3+}$ suggested the electrochemical oxidation of $Co^{2+}$ to $Co^{3+}$ during BA-oxidation to form Co(O)OH.[4–6]

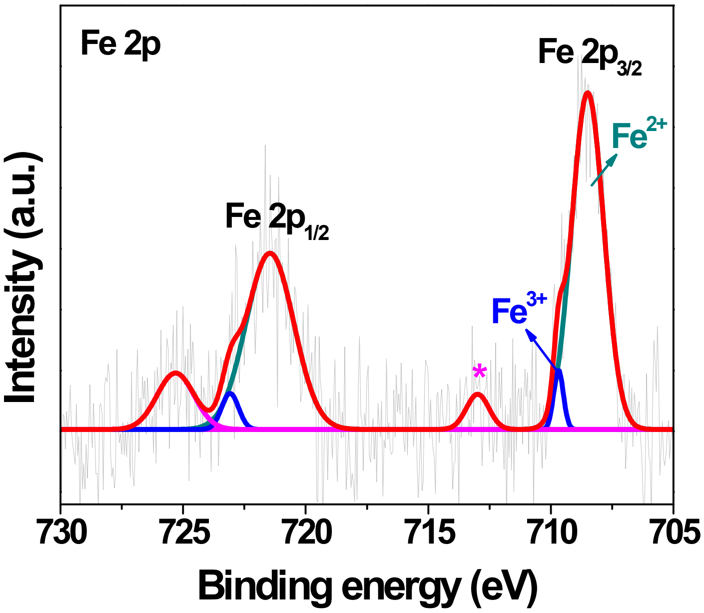

**Figure S28.** Fe 2p XPS spectrum of CoFe-PBA@A-CF after BA-oxidation. The spectrum exhibits two main peaks corresponding to Fe $2p_{3/2}$ and Fe $2p_{1/2}$, with deconvolution of the Fe $2p_{3/2}$ peak revealing two signals at 708.48 eV and 709.67 eV, attributed to $Fe^{2+}$ and $Fe^{3+}$ species, respectively.[4–6]

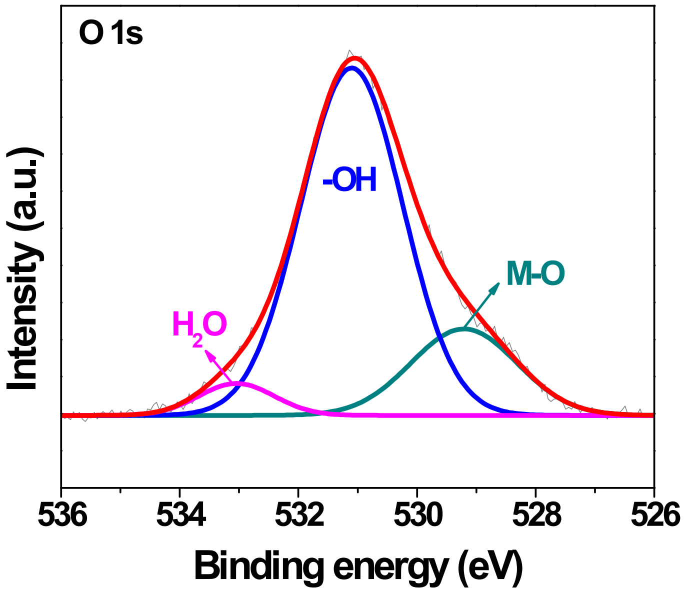

**Figure S29.** O 1s XPS spectrum of CoFe-PBA@A-CF after BA-oxidation. The spectrum exhibits three main peaks at 529.20 eV, 531.10 eV, and 533.06 eV, attributed to M-O bond, surface -OH groups, and adsorbed water molecules, respectively.[4–6]

**Table S2.** The composition of the catalyst (atomic percentage) was measured from EDX and XPS.

| **Catalyst** | **Co (%) (EDX)** | **Co (%) (XPS)** | **Fe (%) (EDX)** | **Fe (%) (XPS)** | **N (%) (EDX)** | **N (%) (XPS)** | **C (%) (EDX)** | **C (%) (XPS)** | **O (%) (EDX)** | **O (%) (XPS)** |
|---|---|---|---|---|---|---|---|---|---|---|
| **CoFe-PBA@A-CF** | 26.45 | 15.56 | 13.92 | 10.26 | 14.38 | 11.41 | 19.25 | 44.22 | 26.00 | 18.56 |
| **CoFe-PBA@CF** | 25.56 | 18.00 | 15.54 | 10.87 | 20.79 | 13.73 | 26.98 | 48.18 | 11.13 | 9.22 |
| **CoFe-PBA@A-CF after BAOR** | 20.53 | 31.90 | 5.56 | 8.13 | - | - | 10.56 | 43.81 | 63.35 | 16.16 |

## References

1. B. Singh, T. Ansari, N. N. Verma, Y.-C. Huang, P. M. Mannu, C.-L. Dong and A. Indra, *J. Mater. Chem. A*, 2024, **12**, 19321-19330.
2. L. Han, P. Tang, Á. Reyes-Carmona, B. Rodríguez-García, M. Torréns, J. R. Morante, J. Arbiol and J. R. Galan-Mascaros, *J. Am. Chem. Soc.*, 2016, **138**, 16037–16045.
3. Z. Chen, B. Fei, M. Hou, X. Yan, M. Chen, H. Qing and R. Wu, *Nano Energy*, 2020, **68**, 104371.
4. X. Meng, J. Yang, C. Zhang, Y. Fu, K. Li, M. Sun, X. Wang, C. Dong, B. Ma and Y. Ding, *ACS Catal.*, 2022, **12**, 89–100.
5. A. A. Ahmad, T. G. Ulusoy Ghobadi, M. Buyuktemiz, E. Ozbay, Y. Dede and F. Karadas, *Inorg. Chem.*, 2022, **61**, 3931–3941.

6. T. Dhanasekaran, A. Bovas, and T. P. Radhakrishnan, *ACS Appl. Mater. Interfaces*, 2023, **15**, 6687–6696.